Epitaxial (100), (110), and (111) $BaTiO_3$ films on $SrTiO_3$ substrates – a transmission electron microscopy study

I.-E. Nylund,[1] T. M. Raeder,[1] P. E. Vullum,[2] and T. Grande[1, a)]

[1)] *Department of Materials Science and Engineering, NTNU Norwegian University of Science and Technology, NO-7491 Trondheim, Norway*

[2)] *Department of Physics, NTNU Norwegian University of Science and Technology, NO-7491 Trondheim, Norway*

(Dated: 12 February 2021)

Chemical solution deposition (CSD) is a versatile method to fabricate oxide films. Here, structure and local variations in the chemical composition of $BaTiO_3$ (BTO) films prepared by CSD on (100), (110), and (111) $SrTiO_3$ (STO) substrates were examined by transmission electron microscopy. The films were shown to be epitaxial and relaxation of the films occurred by formation of edge dislocations at the substrate-film interfaces. The Burgers vectors of the dislocations were determined to be $a\langle 010\rangle$, $a[1\bar{1}0]$ and $a[001]$, and $a\langle 110\rangle$, for the (100), (110), and (111) films, respectively. Due to the difference in thermal expansion between STO and BTO, the films are demonstrated to be under tensile strain. Furthermore, the boundaries between each deposited layer in the BTO films were found to be Ba-deficient in all cases. In case of the (111) oriented film, defects like an anti-phase boundary or a thin layer with a twinned crystal structure were identified at the boundary between each deposited layer. Moreover, a larger grain was observed at the film surface with twinned crystal structure. The interdiffusion length of A-cations at the STO-BTO interface, studied by electron energy-loss spectroscopy, was found to be 3.4, 5.3, and 5.3 nm, for the (100), (110), and (111) oriented films, respectively. Interdiffusion of cations across the STO-BTO interface was discussed in relation to cation diffusion in bulk BTO and STO. Despite the presence of imperfections demonstrated in this work, the films possess excellent ferroelectric properties, meaning that none of the imperfections are detrimental to the ferroelectric properties.

I. INTRODUCTION

$BaTiO_3$ (BTO) is known as one of the prototypic lead-free ferroelectric materials applied in electrical devices due to its excellent dielectric properties[1]. Bulk BTO has a tetragonal crystal structure at room temperature, with cell parameters $a = 3.993$ Å and $c = 4.035$ Å, and a Curie temperature (T_c) of 120 °C[2]. Typically, ferroelectric domains with 90° or 180° domain walls, located on pseudocubic $\{110\}$ and $\{100\}$ planes, respectively, are found in BTO, which can be observed either by optical or electron microscopy[3]. Thin films have become increasingly more important in order to minimize the physical size and energy demand of electronic devices. BTO films can be deposited either by physical deposition techniques, like pulsed laser deposition (PLD)[4,5] or by chemical deposition techniques like chemical solution deposition (CSD)[6,7].

Strain engineering of oxide ferroelectric films is a viable way of controlling and enhancing the functional properties, e.g. increasing the Curie temperature (T_c). There are multiple ways of straining a ferroelectric film. Most common for thin films grown via atomic layer-by-layer deposition, is epitaxial strain engineering, utilizing the lattice parameter mismatch between the substrate and the thin film[8,9]. In BTO grown on $DyScO_3$ enhancement of ferroelectricity was demonstrated under compressive strain, where T_c was increased by about 500 °C and the remnant polarization increased by 250 %[10]. Coherent epitaxially strained BTO on $SrTiO_3$ (STO) is under compressive strain since the lattice parameter of BTO is larger than the lattice parameter of STO ($a_{STO} = 3.905$ Å[2]). In this case the polar c-axis points perpendicular to the film surface since this crystal orientation minimizes the lattice mismatch between substrate and film. However, thin films can only be strained epitaxially up to a certain film thickness, depending on the magnitude of the lattice mismatch, before dislocations are introduced and the crystal lattice of the film relaxes. In the case of BTO grown on (100) STO, it has been shown that the critical thickness is 5 nm or less[5].

Another way of introducing strain is to utilize the difference in thermal expansion coefficient between the substrate and the film. This is known as thermal strain, and it was demonstrated that tensile strain was introduced in thick BTO films (>200 nm) grown on STO, where the polar axis aligned in-plane[6]. The same films are subject to the present study. The dielectric and ferroelectric properties of these films have been reported in detail, including the determination of the domain pattern by piezoresponse force microscopy (PFM)[11]. However, the structure and the effect of the CSD processing method on the film quality remains to be investigated.

Transmission electron microscopy (TEM) is a powerful tool which can be used to investigate both structural and chemical properties down to atomic scale. Here, we present a thorough study of the structure of BTO films on STO substrates. The BTO films, with in-plane tensile strain, were synthesized by CSD on (100), (110) and (111) oriented STO substrates[11] TEM was utilized to study how the CSD technique affects the structure and chemistry of the three differently oriented films at the nanoscale. Specifically, the degree of epitaxy and dislocations at the STO-BTO interface were studied by electron diffraction and imaging. Furthermore, local variations in chemical composition across the STO-BTO interface, as well in the interior of the BTO films, were investigated by electron

[a)] Corresponding author: grande@ntnu.no

energy-loss spectroscopy (EELS). Despite the present observations of several types of defects and inhomogeneities, the corresponding films possess excellent ferroelectric properties, like high remnant polarization and an enhanced T_c[11].

II. EXPERIMENTAL

A. BTO film processing

BTO films were prepared by aqueous CSD based on $Ba(NO_3)_2$ and Ti-isopropoxide cation precursors. Ethylenediaminetetraacetic acid (EDTA) and citric acid were used as complexing agents, and ammonia solution was used to increase the pH. All chemicals were obtained from Sigma-Aldrich St. Louis, MI, USA. The solution was adjusted to a concentration of 0.13M and spin coated onto (100), (110), and (111) oriented STO substrates (Crystal GmbH, Berlin, Germany). In total, eight layers were deposited, where each layer was heat treated from ambient temperature with a heating rate of 100 °C/min to 450 °C, then at 50 °C/min to 550 °C, and lastly at 20 °C/s to 1000 °C where it was held for 5 minutes after the deposition of each layer. The CSD process is described in further detail elsewhere[6,11].

B. TEM analysis

The TEM specimens were prepared using a FEI Helios G4 UX focused ion beam (FIB) with an EasyLift EX NanoManipulator. A carbon protection layer was deposited on top of the area of interest prior to ion-milling. The first part of the protection layer was deposited by electron beam assisted deposition to avoid any Ga^+ induced damage of the BTO film. Coarse thinning was performed at 30 kV acceleration voltage for the Ga^+ ions. In the final thinning steps, 5 kV and lastly to 2 kV was used on either side of the lamella to minimize the thickness of the surface damaged layer.

The TEM analysis was carried out on a double Cs aberration corrected cold FEG JEOL ARM200F, operated at 200 kV. The ARM is equipped with a Quantum ER GIF for fast dual EELS. Diffraction patterns (DPs) were acquired using a selected area aperture where the substrate-film interface was placed approximately in the middle of the aperture, such that diffraction from both the STO substrate and BTO film were included in each DP. The in-plane (IP) and out-of-plane (OOP) lattice parameters for all the differently oriented BTO films were measured in Digital Micrograph. The STO diffraction spots were used as internal references, assuming that the substrate lattice parameter equals that of single crystal STO. The orientations along which the in-plane and out-of-plane lattice parameters were measured are presented in Tab. I. In order to compare lattice parameters across differently oriented films, they are presented as $d/|d|$, where $|d|$ is the length of the unit vectors along different crystallographic axes, assuming a cubic symmetry. $|d|$ along the different crystallographic axes is included in Tab. I.

TABLE I. The orientations, along which the in-plane (IP) and out-of-plane (OOP) lattice parameters in the BTO films were measured. See Fig. 2 for indexed DPs.

Film	d_{IP}	$\lvert d_{IP}\rvert$	d_{OOP}	$\lvert d_{OOP}\rvert$
(100)	$[010]$	1	$[100]$	1
(110)	$[1\bar{1}0]$	$\sqrt{2}$	$[110]$	$\sqrt{2}$
(111)	$[11\bar{2}]$	$\sqrt{6}$	$[111]$	$\sqrt{3}$

Scanning TEM (STEM) imaging was performed using a beam semi-convergence angle of 27 mrad. Bright-field STEM (BF-STEM) images were acquired with an outer semi-collection angle of 33 mrad, while the simultaneously acquired high-angle annular dark-field STEM (HAADF-STEM) images were taken with semi-collection angles of 51-203 mrad (Fig. 4, 5, 6 and 9(a)). The other HAADF-STEM images (Fig. 1, 8, 9(b)) were taken with semi-collection angles of 118-471 mrad, to promote pure Z-contrast and minimize diffraction and strain contrast. STEM-EELS was performed with a beam current of 66 pA, a beam semi-convergence angle of 27 mrad, while the semi-collected angle into the GIF was 67 mrad. The HAADF-STEM images accompanying the EELS data were taken with semi-collection angles of 118-471 mrad. EELS maps were acquired with a step size of 0.4 Å with 0.01 s or 0.02 s dwell time in each probe position. The energy dispersion was 1 eV/ch. At the STO-BTO interface, the EELS maps were acquired between the misfit dislocations, to minimize diffusion effects caused by the dislocations.

C. Data analysis

The EEL spectra were collected as maps and analyzed by the Gatan Digital Micrograph EELS Analysis package to determine the relative composition of Sr and Ba. Each compositional map was then binned perpendicular to the feature of interest for further analysis. The Python packages HyperSpy[12], SciPy[13], and Matplotlib[14] were then used to load, fit, and plot the data, respectively. In order to determine the length scale of the interdiffusion of Sr and Ba at the substrate-film interface, and thereby determine the width of the interface, the four parameter logistic regression function in Eq. 1 was used as mathematical model to fit the experimental concentration profiles of Sr and Ba:

$$f(x) = \frac{A-D}{1+(x/C)^B} + D. \tag{1}$$

Here, x is the independent variable, and the parameters A, B, C, and D were fitted using non-linear least squares regression. The concentration profiles were then normalized based on this fit, assuming that STO and BTO were stoichiometric sufficiently far from the interface ($> 3-4$ nm from the intersection of the two concentration profiles).

The interdiffusion distance was found by determining the distance from 0 to 1 normalized concentration for the Ba profiles, where the start and end points of the interdiffusion region were defined to be between 0.02 and 0.98 normalized concentration of Ba. Specimen drift during the acquisition of the EEL

spectra was corrected by comparing the experimental and theoretical values of the lattice spacing along the interface normal in the HAADF-STEM images which were acquired simultaneously with the EEL spectra. The relative thickness t/λ was measured by EELS and found to be 0.7, 0.4, and 0.7, for the (100), (110), and (111) lamellae, respectively.

III. RESULTS

A. Film morphology and relaxed epitaxy

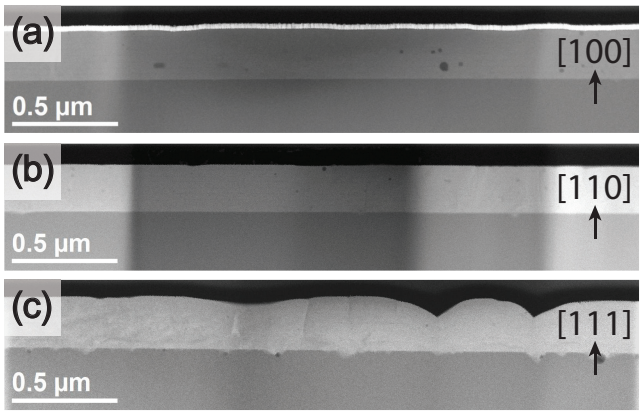

FIG. 1. HAADF-STEM images showing the cross section of the three differently oriented films (a) (100), (b) (110), and (c) (111). Vertical contrast differences occur because of varying lamella thickness, created by the FIB specimen preparation method. The (100) and (110) films show uniform thickness, whereas the thickness of the (111) oriented film varies. The thin, bright contrast layer directly above the BTO film in (a) is Pt/Pd that was sputter coated on top of the sample prior to FIB preparation in order to avoid charging.

Scanning electron micrographs (Fig. S1) of the three BTO films demonstrated that the (100) and (110) BTO films possessed smooth surfaces, whereas the surface of the (111) BTO film was inhomogeneous with a pronounced roughness in certain areas. Cross-sectional TEM lamellae were prepared from arbitrary regions of (100) and (110) BTO films, and the cross-sectional lamella from the (111) film was prepared to include regions with both smooth and rough surfaces. HAADF-STEM images of the cross sections are shown in Fig. 1. The images of the (100) and (110) films demonstrate that they have a uniform thickness of $t = 230 \pm 4$ nm and $t = 218 \pm 2$ nm, and that the thickness of the (111) film is less uniform: $t = 220 \pm 27$ nm.

The selected area diffraction patterns (SADPs) from the three BTO films are shown in Fig. 2. The SADPs are rotated corresponding to the orientations of the films in Fig. 1, i.e. with the film surface upwards. Visible in all the SADPs is a splitting between two sets of diffraction spots: One set corresponding to diffraction from STO, and the second set corresponding to the BTO film. The SADPs from the films and substrates show the same orientation, demonstrating that the films are epitaxial to the crystallographic orientation of the substrates. The splitting between the diffraction spots along all directions demonstrates that the films have relaxed compared to the substrates. The measured in-plane and out-of-plane lattice parameters are presented in Tab. II. All the in-plane and out-of-plane lattice parameters of the BTO films are intermediate to the a and c parameter of single crystal BTO, meaning that the films are under tensile strain. This was also demonstrated by reciprocal space mapping of the same film system previously[6,11]. In each diffraction pattern in Fig. 2, a pair of diffraction spots are enlarged and highlighted in the insets (red). For all films, the BTO spots are drawn out normal to the radial direction, however, the spread is only within 1°.

TABLE II. In-plane (IP) and out-of-plane (OOP) lattice parameters of the BTO films determined by TEM.

Film	IP $d \pm \Delta d$ (Å)	OOP $d \pm \Delta d$ (Å)
(100)	4.02 ± 0.01	4.02 ± 0.01
(110)	$(4.01 \pm 0.01)/\sqrt{2}$	$(4.00 \pm 0.01)/\sqrt{2}$
(111)	$(4.01 \pm 0.01)/\sqrt{6}$	$(4.01 \pm 0.01)/\sqrt{3}$

B. Periodic misfit dislocations and Burgers vectors

Figure 3 displays a BF-STEM image of the STO-BTO interface in the (100) film. Misfit dislocations, seen by strain contrast (highlighted by yellow arrows), are clearly present at the interface. The presence of dislocations at the STO-BTO interface evidence that the epitaxial strain due to lattice mismatch is relaxed by formation of dislocations at the interface. Similar images for the (110) and (111) films are shown in Fig. S2 in the supporting information. The distance between each dislocation is quite periodic, particularly in the case of the (100) film, were the distance was found to be 14.5 ± 1.4 nm. In the case of the (110) and the (111) films, the periodic dislocations were imaged from two different orientations, due to the in-plane anisotropy of the higher index substrates. In the (110) film the dislocation spacing was found to be 18.4 ± 2.5 nm and 15.2 ± 2.6 nm, when viewed along beam direction $[00\bar{1}]$ and $[1\bar{1}0]$, respectively. In the (111) film the dislocation spacing was found to be 15.7 ± 3.2 nm and 15.3 ± 4.4 nm, when viewed along beam direction $[\bar{1}10]$ and $[11\bar{2}]$, respectively. In the case of the (111) film with beam direction $[11\bar{2}]$, the BF-STEM contrast was so poor that high-resolution images including two dislocations were acquired, and the distance between two and two dislocations were measured in multiple images.

A high-resolution HAADF-STEM image of the dislocations observed in the (100) film is shown in Fig. 4. Constructing a Burgers closure around the dislocation reveals that the Burgers vector is $a[010]$. Only dislocations with Burgers vector $a\langle 010\rangle$ were observed in the (100) film. Similar types of high-resolution HAADF-STEM images for the (110) and (111) films are shown in Fig. 5 and 6, where the dislocation-types which were most frequently observed are displayed. A few other types of dislocations, which were not analyzed further, were also observed. In the case of the (110) and (111)

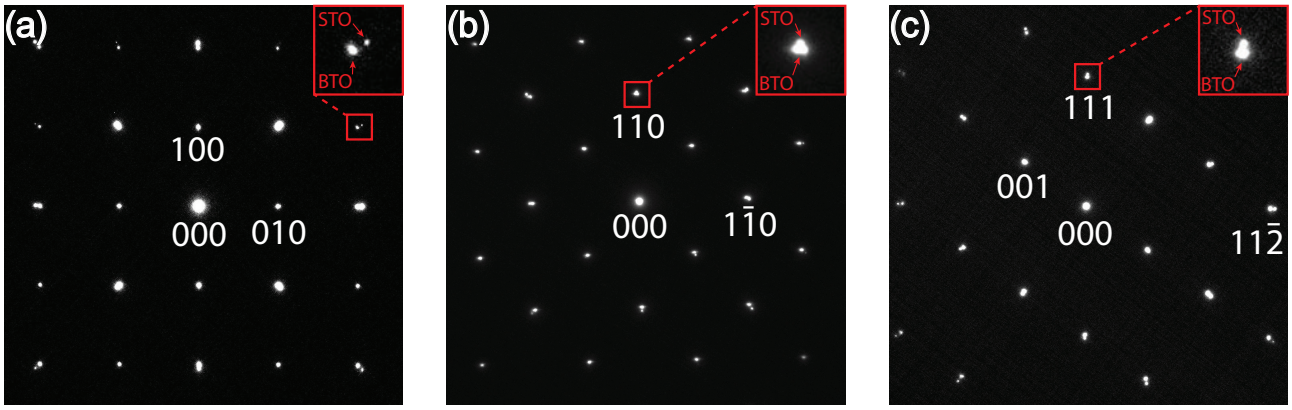

FIG. 2. SADPs from the (a) (100), (b) (110), and (c) (111) oriented films and substrates. The DPs are rotated corresponding to Fig. 1, i.e. with the film surface pointing upwards. The red boxes indicate a highlighted and enlarged set of BTO and STO diffraction spots for each film orientation. The STO spots are circular, while the BTO spots are somewhat non-circular and distorted.

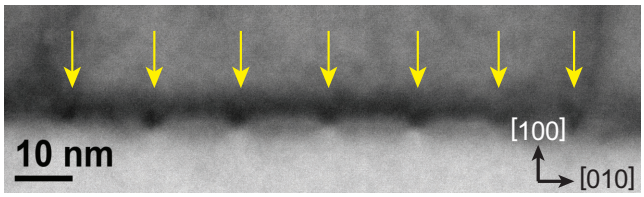

FIG. 3. BF-STEM image displaying strain contrast originating from misfit dislocations at the substrate-film interface in the (100) film.

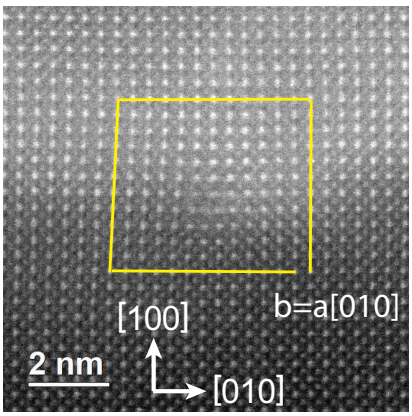

FIG. 4. High-resolution HAADF-STEM image displaying a misfit dislocation with Burgers vector $\vec{b} = a[010]$ at the STO-BTO interface.

films, the dislocations are imaged from two different orientations to clarify the structural detail of the dislocations, as the Burgers vectors might have a component along the beam direction. Burgers closures were also constructed for the (110) and (111) films, and the projected Burgers vectors were determined to be $a[1\bar{1}0]$ and $a[001]$, for the two different projections in the (110) film, and $\frac{1}{2}a[11\bar{2}]$ and $a[1\bar{1}0]$ for the two different projections in the (111) film. However, the $\frac{1}{2}a[11\bar{2}]$ Burgers vector is just a projection, i.e. it has a component parallel to the beam direction, as misfit dislocations in perovskite-based films usually have a perfect Burgers vector of $a\langle 100\rangle$ or $a\langle 110\rangle$[15]. The atomic structures below the images in Fig. 6 clarifies the possible Burgers vector, since it is determined as the only common possible Burgers vector based on the two images taken along two different crystallographic directions. In this case, the Burgers vector in the (111) film is $a\langle 110\rangle$.

C. Chemical analysis of STO-BTO interface

Compositional analysis by EELS was performed across the STO-BTO interface. Representative normalized concentration profiles of Sr and Ba across this interface for the (100), (110), and (111) films are shown in Fig. 7. Measurements at six different locations in the (100) and (110) films, and four locations in the (111) film, give average interdiffusion distances of 3.4 ± 0.5 nm, 5.3 ± 1.4 nm, and 5.3 ± 0.2 nm, respectively. This means that the Sr/Ba interdiffusion extends over a length corresponding to 8-13 unit cells. This can be related to the diffusion constant D by the simple relation:

$$D = \frac{x^2}{\tau}, \tag{2}$$

where x is the interdiffusion distance, and τ is the time the films were kept at high temperature during processing. Applying Eq. 2 to calculate the diffusion constants for the different orientations, where $\tau = 5 * 8$ minutes, gives

$$D_{100} = 4.8 \times 10^{-17}\ \mathrm{cm}^2/\mathrm{s}$$
$$D_{110} = 1.2 \times 10^{-16}\ \mathrm{cm}^2/\mathrm{s}$$
$$D_{111} = 1.2 \times 10^{-16}\ \mathrm{cm}^2/\mathrm{s},$$

which is $\sim 10^2$ times lower than reported for Ba diffusion in bulk BTO[16], and $\sim 10^4$ times higher than Sr diffusion in STO[17].

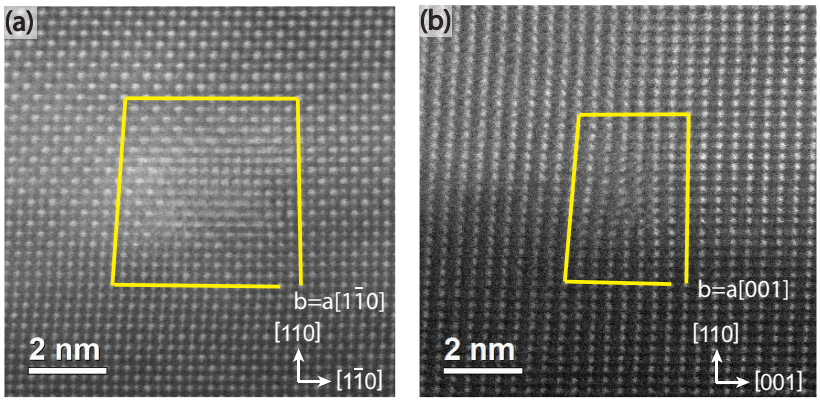

FIG. 5. High-resolution HAADF-STEM images of misfit dislocations in the (110) film imaged along the beam direction (a) $[00\bar{1}]$ and (b) $[1\bar{1}0]$. The Burgers closures demonstrate that the Burgers vectors are (a) $a[1\bar{1}0]$ and (b) $a[001]$.

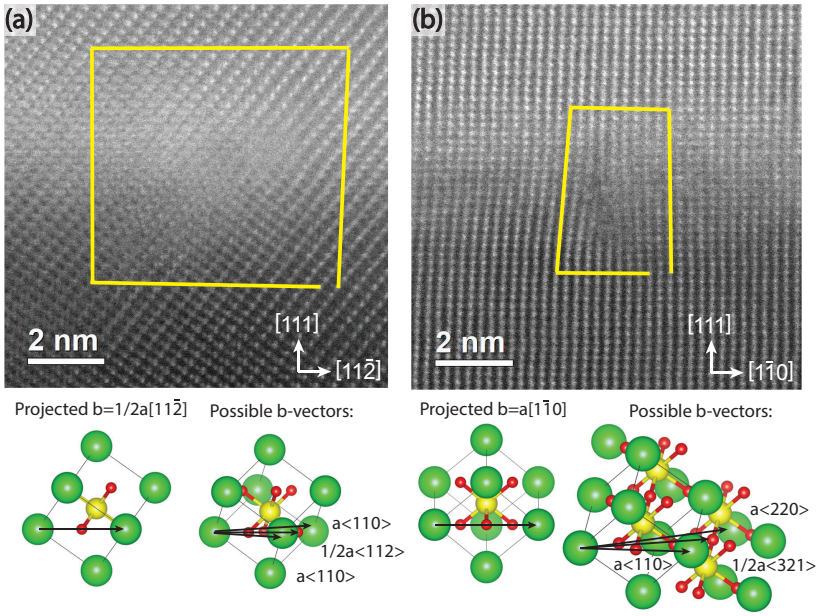

FIG. 6. High-resolution HAADF-STEM images of misfit dislocations in the (111) film imaged along the beam direction (a) $[\bar{1}10]$ and (b) $[11\bar{2}]$. Included are atomic structure figures which elaborate on the possible Burgers vector for the misfit dislocations in the (111) film. Here it is demonstrated that $\vec{b} = a\langle 110\rangle$.

D. Boundaries between spin coated layers

The films were prepared by multiple spin coatings, and the individual layers formed by CSD could be identified by TEM. Figure 8(a, c, e) shows HAADF-STEM images of a representative part of the cross section of the BTO films. Visible in these images are darker lines which are parallel to the film surface. The thickness of each spin coated layer is $\sim 20-30$ nm, and the dark lines correspond to the boundary between each spin coated layer. High-resolution images of the areas marked with blue boxes in 8(a, c, e) are displayed in Fig. 8(b, d, f). Clearly visible in the middle of all the high-resolution images is a band where the atomic columns have darker contrast. The Z-contrast of HAADF-STEM images indicate that the darker areas are layers with lower Ba content. This was confirmed by EELS (Fig. S3), which demonstrates a significant Ba-deficiency at the boundary between each CSD layer corresponding to the darker contrast in Fig. 8. It is also evident in Fig. 8 that the perovskite crystal remains intact without observable structural defects across the boundaries between the CSD layers. This was the case for all the thin dark lines observed in the (100) and (110) films, but not for all cases of the (111) film.

Cross-sectional BF- and HAADF-STEM images of the (111) film are shown in Fig. 9(a and c), respectively. High-resolution HAADF-STEM images of the borderline between the CSD layers in the (111) film are displayed in Fig. 9(b and d), from the areas marked with blue boxes in Fig. 9(a and c). Here, the crystal structure is modified across the borderline between the two CSD layers. In Fig. 9(b) there is a thin layer

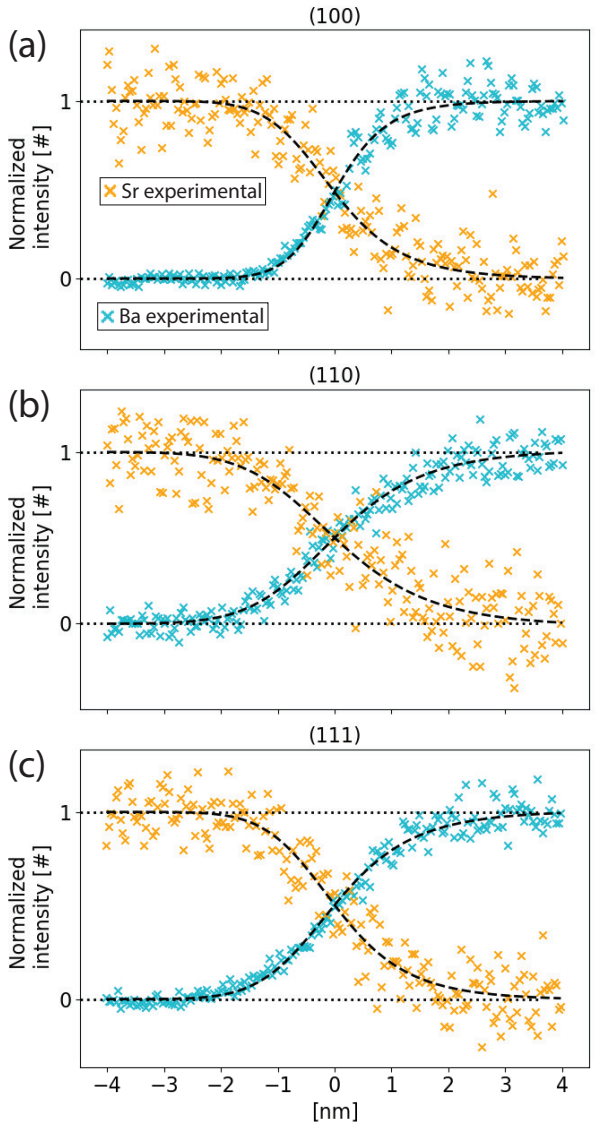

FIG. 7. Normalized Ba and Sr EELS profiles across the (a) (100), (b) (110) and (c) (111) oriented STO-BTO interfaces. Experimental values for Ba is shown in light blue, and experimental values are in orange for Sr. The black dashed lines are the fit from eq. 1. Horizontal dotted lines are guides at normalized values of 0 and 1.

where the crystal is twinned around the (111) plane compared to the rest of the film. In Fig. 9(d) the red dashed line follows an atomic column below the internal interface and a gap between atomic columns above. This is known as an anti-phase boundary (APB), wherein the crystal structure remains the same on both sides of the boundary. It is however shifted by half a unit cell along the [001] direction by crossing the APB.

Figure 9(e) shows a dark-field TEM (DF-TEM) image of the (111) film, acquired by centring the objective aperture around the 100 spot indexed with red in the diffraction pattern in Fig. 9(f). It is clearly visible that only a certain part of the film is bright in Fig. 9(e), meaning that this part of the

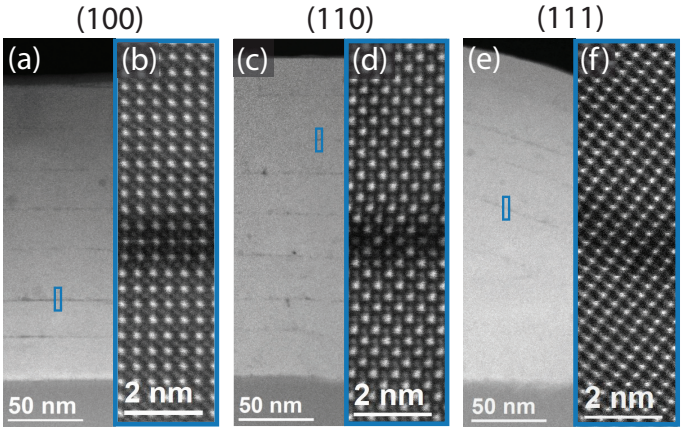

FIG. 8. Z-contrast HAADF-STEM images showing darker layers in the (100) (a and b), (110) (c and d), and (111) (e and f) BTO film.

film has a different crystallographic orientation than the rest of the film. This "grain" is twinned compared to the rest of the film, with the (111) plane as the twinning plane. All Bragg spots in the twinned grain (indexed in red) can be found by reflecting all Bragg spots from the rest of the film (indexed in white) along the (111) mirror plane, i.e. around the red dashed line shown in Fig. 9(f). The thin, twinned lamella seen in Fig. 9(b) at the boundary between two spin coated layer has the same twinning as the larger grain observed in Fig. 9(e). The crystallographic relationship between the film and the grain is also equivalent to a 60° rotation around the [111] axis. A few other defects were observed in the films, e.g. voids visible in Fig. 1(a) and 1(b). They were not studied further and are not included in this work.

IV. DISCUSSION

A. Epitaxy, strain state and ferroelectric domains

Aqueous CSD is a simple, scalable, and environmentally friendly processing route for textured oxide films. It is further possible to tailor the degree of texture and the structure by controlling the heating profile and heating rate for pyrolysis and nucleation[18]. The TEM work shown here demonstrates the nature of the structure and chemistry of BTO films prepared by CSD, including imperfections and defects. Despite these imperfections, the epitaxial films possess impressive ferroelectric properties[11], meaning that none of the imperfections are detrimental to the ferroelectric properties.

For example, it is demonstrated that misfit dislocations are present and that the films are under tensile strain which can be explained by the following: Due to the difference in lattice parameter between STO and BTO, BTO is under compressive strain at the crystallisation temperature of 1000 °C. Each spin coated layer is much thicker than the critical thickness for coherently strained BTO on STO[5], and thus the film is relaxed by misfit dislocations. During cooling, the thermal contraction of STO is smaller than for BTO[2]. Hence, if the

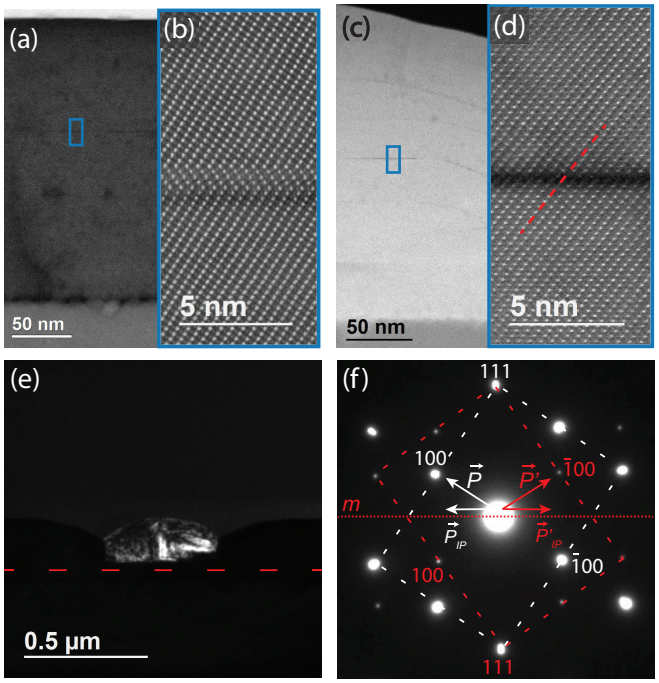

FIG. 9. Interfaces and grain only observed in the (111) oriented film. (a) BF-STEM image of the cross section of the (111) film, where a darker horizontal line is observed and marked with a blue rectangle, (b) magnification of the area in the blue rectangle in (a) where a thin crystallographic twin layer is observed. (c) HAADF-STEM image showing a clear dark horizontal line which is marked with a blue square and magnified in (d) where an APB is present. (e) DF-TEM image acquired from the 100 spot marked with red in the DP in (f). The red dashed line in (e) indicate the substrate-film interface. Also indicated in the DP (f) is the mirror relation between the film (indexed with white) and the grain (indexed with red).

misfit dislocations are pinned and cannot move, BTO will experience a gradually increasing tensile strain caused by the STO substrate[5]. At the ferroelectric phase transition temperature, the long polar axis will align parallel to the STO-BTO interface in order to minimize the tensile strain. In the (100) film, polarization along [010] and [001] will be equivalent, and a 90° domain pattern is formed. Similarly, the macroscopic polarization is aligned mainly in-plane in the (110) and (111) films, with a more complicated domain pattern[11]. This demonstrates an alternative route for strain engineering of thin films, where changing either the crystallization temperature or choosing substrates with different thermal expansion coefficients is a way of controlling the amount of strain introduced in the film, and thus also affecting the polarization state of the film.

It was not possible to observe splitting between diffraction spots from different domains in these films, as demonstrated by the diffraction patterns taken by only including the film in the selected area aperture in Fig. S4, S5, and S6. This is likely due to the very similar in-plane and out-of-plane lattice parameters. The shape of the diffraction spots (in the red boxes in Fig. 2), evidence a broadening in the 120, 110, and 111 BTO spots in the (100), (110), and (111) oriented films, respectively, which is suggested to be connected to the ferroelectric domain structure of the films.

B. Periodic misfit dislocations and Burgers vectors

The theoretical spacing S between the edge dislocations in a film on a rigid substrate can be calculated by

$$S = b/(\delta - \varepsilon), \tag{3}$$

where b is the in-plane component of Burgers vector perpendicular to the line direction $\vec{l}$ of the misfit dislocation, $\delta = (a_f - a_s)/a_s$ is the misfit parameter between the film (a_f) and substrate (a_s), and ε is the residual in-plane strain present in the film[19]. In order to analyze the dislocation spacing, the line direction $\vec{l}$ of the misfit dislocation must be known. The dislocation core will look sharp if the line direction is viewed "edge-on", i.e. when the dislocation line is the same as the beam viewing direction[20]. This is the case for the misfit dislocations found in the (100) film, where the line direction is determined as $\vec{l} = \langle 001 \rangle$ and the misfit dislocation is of pure edge type, where the Burgers vector is always perpendicular to the line direction. Assuming that there were no residual strains present in the film at the crystallization temperature, the theoretical spacing between the edge dislocations (calculated at 1000 °C, and corrected by thermal expansion to room temperature values) would be 15.6 nm, where lattice parameters for STO and BTO at 1000 °C is taken from the work by Taylor[2]. The experimental value fits the theoretical value within the standard deviation, demonstrating that the film is relaxed by the introduction of edge dislocations. Langjahr *et al.*[21] have grown the perovskite $SrTi_{0.5}Zr_{0.5}O_3$(STZO) on STO by CSD and heat treated it at 1000 °C for 1 h. STZO-STO has approximately the same lattice mismatch as BTO-STO, and it was also shown that the Burgers vector in the STZO-STO system were of $a\langle 010 \rangle$-type, with line direction of $\langle 001 \rangle$. Giving the same theoretical dislocation spacing for a relaxed film, and a measured spacing of 16.1±5.4 nm, demonstrating that the simple relation in Eq. 3 holds for relaxed films across different chemical compositions.

For the (110) film, the line direction is clearly viewed "edge-on" for beam, and hence, line direction $[1\bar{1}0]$ (Fig. 5(b)). The dislocation core for the beam direction $[00\bar{1}]$ also looks fairly sharp (Fig. 5(a)), so it is also determined as a line direction, where the strong lattice distortion around the dislocation is assumed to be the cause for the blurring in the image[22]. This means that the (110) film has two types of misfit dislocations, each with different line direction and Burgers vectors. The line directions are perpendicular to each other, and the respective Burgers vectors are of pure edge type, which relax the in-plane strain in the two anisotropic orthogonal directions in the (110) film. First, $\vec{l} = [00\bar{1}]$ and $\vec{b} = a[1\bar{1}0]$ gives a theoretical dislocation distance of 22.0 nm, and $\vec{l} = [1\bar{1}0]$ and $\vec{b} = a[001]$ gives a theoretical dislocation distance of 15.6 nm, where calculations were performed the same way as described previously. The experimental values are 18.4 ± 2.5 nm and 15.2 ± 2.6 nm, respectively, demonstrating that strain is also relaxed due to introduction of edge

dislocations in the (110) film. Dislocations are observed to occur more frequent than the theoretical prediction for $\vec{b} = [1\bar{1}0]$, this might for example be caused by a small miscut angle of the substrate. The situation for the (110) STO-BTO system here is different from the dislocation system observed in the (110) $Nd_{0.45}Sr_{0.55}MnO_3$ film on STO, where misfit dislocations were found along the interface with line directions of both $\langle 111 \rangle$ and [001], with Burgers vector of $a\langle 110 \rangle$-type[20].

Tang *et al.* performed an analysis of the formation mechanism of misfit dislocations with Burgers vector of $a\langle 110 \rangle$ on (111) oriented perovskites which infers that the misfit line directions should run along the $\langle 112 \rangle$ directions[20]. This is further demonstrated by Xu *et al.* for (111)$PbTiO_3$ (PTO) on $LaAlO_3$ (LAO)[15], and it is also shown here in Fig. 6(b) that the dislocation core is sharp (i.e. viewed "edge-on") when viewed along $[11\bar{2}]$. Taking $a[0\bar{1}1]$ as an example for the Burgers vector in the (111) film, it can be decomposed as:

$$a[0\bar{1}1] = \frac{1}{2}a[1\bar{1}0] + \frac{1}{2}a[\bar{1}\bar{1}2], \tag{4}$$

where $\frac{1}{2}a[1\bar{1}0]$ is perpendicular to the direction of the dislocation line, and $\frac{1}{2}a[\bar{1}\bar{1}2]$ is parallel to the direction of the dislocation line. Meaning that the former is a pure edge component which could relax lattice mismatch along $(1\bar{1}0)$ planes, while the latter is a pure screw component which could relax shear strains[15]. Calculating the theoretical spacing between edge dislocations with $\vec{b} = \frac{1}{2}a[1\bar{1}0]$ gives $S = 11$ nm, whereas the measured dislocation density in the (111) film is 15.7 ± 3.2 nm and 15.3 ± 4.4 nm, when viewed along the beam direction $[\bar{1}10]$ and $[11\bar{2}]$, respectively. The deviation between theoretical and measured distances can be explained by the fact that the $\langle 112 \rangle$ directions have a tree-fold symmetry in the (111) film, meaning that $[\bar{2}11]$ and $[1\bar{2}1]$ are not perpendicular to $[11\bar{2}]$. The misfit dislocations with Burgers vectors along the respective $\langle 110 \rangle$ directions for line directions $[\bar{2}11]$ and $[1\bar{2}1]$ will therefore have a component which contributes to in-plane relaxation along $[1\bar{1}0]$. Consequently, to relax the film completely, fewer dislocations are needed, thus the distance between them becomes larger, which is what is measured for the (111) film. The discussion of the dislocations observed in this work is summarized in Tab. III.

TABLE III. Summary of the pure *edge components* of the Burgers vectors and line directions, and the dislocation spacing in the three differently oriented films. See text for decomposition of the Burgers vector in the (111) film.

Film	Burgers vector (edge component)	Line direction	S_{theory} [nm]	$S_{\text{experiment}}$ [nm]
(100)	$a\langle 010 \rangle$	$\langle 001 \rangle$	15.6	14.5 ± 1.4
(110)	$a[1\bar{1}0]$	[001]	22.0	18.4 ± 2.5
	a[001]	$[1\bar{1}0]$	15.6	15.2 ± 2.6
(111)	$\frac{1}{2}a[1\bar{1}0]$	$[11\bar{2}]$	11.0[a]	15.3 ± 4.4

[a] See text for explanation of deviation

C. Chemical abruptness at perovskite hetero-interfaces

The diffusion constants calculated for the Sr-Ba interdiffusion at the substrate-film interface are intermediate to the values for Ba diffusion in BTO[16] and Sr diffusion in STO[17], demonstrating that the interface width of hetero-interfaces in perovskites can be estimated by the knowledge of A-cation diffusion constants in the native materials. Cation diffusion in perovskites is mediated by A-cite vacancies[17,23], thus to explain the difference in diffusion constant which is observed between the differently oriented films, the possible paths from one A-site to a vacant A-site in the lattice must be considered. A schematic representation of the possible diffusion paths is shown in Fig. 10. Figure 10(a) shows a 3D sketch of the perovskite unit cell, with three possible straight paths labelled I, II and III, which are perpendicular to the interfaces of the (100), (110), and (111) films, respectively. Path I is an unobstructed path, whereas path II is obstructed by the O-anion, and path III is obstructed by the Ti-cation. Assuming that the most likely diffusion path is along $\langle 100 \rangle$, i.e. along the family of path I, as this is an unobstructed path, and taking only a simple jump mechanism into account, one, two, and three jumps would be necessary to cover a distance of a, $\sqrt{2}a$ and $\sqrt{3}a$, normal to the surface of the (100), (110), and (111) films, respectively. This means that the length covered relative to the number of jumps needed is the longest for the (100) film, i.e. the diffusion length for the (100) is expected to be the longest. However, the shortest interdiffusion distance is measured for (100). It is worth noting that the relative thickness t/λ of the TEM lamellae were similar and reasonably low for all the three cases, with values of 0.7, 0.4 and 0.7 for the (100), (110) and (111) films, respectively. This implies that artificial broadening of the interdiffusion due to the lamella thickness is most severe in the (100) and (111) films. Taking beam broadening into account, the interdiffusion lengths Δ in order of size have this relation: $\Delta_{110} > \Delta_{111} > \Delta_{100}$. Demonstrating that taking only jumps along $\langle 100 \rangle$ into account is not sufficient to properly describe the orientational dependence on the interdiffusion length. The jump possibility along $\langle 100 \rangle$ was also assumed to be the same for all the films/substrates. However, as this diffusion mechanism relies on A-site vacancies in both BTO and STO, the concentration of these vacancies are crucial to the rate of diffusion. Among others, surface termination may affect the number of Sr vacancies in the different substrates.

D. Internal boundaries in all films and structural distortions specific to the (111) film

Thin, Ba-deficient layers are observed at the interfaces between the spin coated layers in all the BTO films (Fig. 8), irrespective of the STO orientation. This is an interesting observation, which can be due to Ba-deficiency introduced during processing of the films. Between each layer, the BTO surface was exposed to air at 1000 °C before this surface was coated with the next BTO layer, and the thermal processing was repeated. Each layer is approximately 20-30 nm thick,

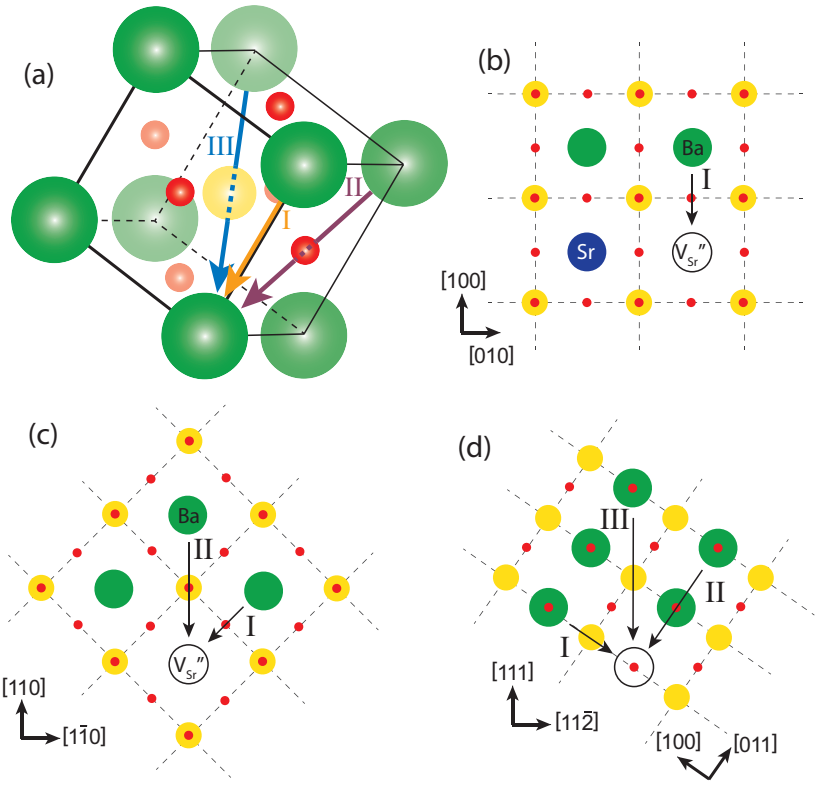

FIG. 10. Possible diffusion paths in the perovskite structure. (a) Schematic showing possible paths in a 3D sketch. I along the cube edge, II along the cube face diagonal, and III along the cube body diagonal. (b), (c), and (d) are 2D sketches of the (100), (110) and (111), respectively, with potential diffusion paths indicated.

and we propose that the lower Ba-content at the boundary between each layer originate from loss of BaO at the outer surface in each thermal processing step. BaO-loss is well known in bulk $BaZrO_3$[24,25], and the present work indicates that BaO-loss is also taking place at temperatures as low as 1000 °C. Over time the Ba-deficiency should diminish due to diffusion of Ba, but the relatively short time at 1000 °C during processing is not sufficient to allow for that. A-site deficiency is also a well-known phenomenon in other ferroelectric oxides such as $BiFeO_3$ (loss of Bi_2O_3)[26], PZT (loss of PbO)[27], and $KNbO_3$ (loss of K_2O)[28]. Similar dark lines can also be observed in the bottom half of the BTO film deposited by CSD on Si(001) with a 2 nm template layer of STO in the work by Edmondson *et al.*[7].

A potential explanation for the occurrence of the APB in the (111) film (Fig. 9(d)) could be that after each spin-coated layer and successive heat treatment, many surface and near-surface defects are introduced, including Ba-vacancies (as demonstrated previously). In order to compensate for these Ba vacancies, at an atomic level, Ti^{4+} takes the place of Ba^{2+} and the unit cell thus shifts by a half in the $\langle 100 \rangle$ direction. It is worth noting that an APB does not affect ferroelectric properties, as it is purely translational in nature.

Regarding the thin twin layer and the twinned grain in the (111) film, they are suggested to originate due to the same mechanism. It is previously demonstrated in perovskites ($SrRuO_3$, BTO, and PZT) that twins which are rotated 60° around the [111] axis occur frequently in thin films grown on substrates with large lattice mismatch, which is also the case for the STO-BTO films studied here. The twin occurs due to stacking faults, where each successive (111) plane is translated by $\frac{1}{3}[11\bar{2}]$. If the crystal twins such that the A-O planes (in an ABO_3 perovskite) form the twin interface, as is evident in Fig. 9(b), the BO_6 octahedra are preserved[29]. Furthermore, twins can relax strain and affect the total net polarization in the thin film. Assuming that the polarization lies along the principal axes in the BTO film, one possibility is that the polarization changes from P to P', as indicated in Fig. 9(f), i.e. the in-plane component of the ferroelectric polarization changes direction by 180° by crossing the twin domain wall. In Fig. 9(f) it is demonstrated for polarization along the pseudo cubic [100] direction. However, the same arguments hold if the polarization should be along the pseudo cubic [010] or [001] directions. Hence twinning can cancel out or reduce the macroscopic in-plane polarization, while the macroscopic out-of-plane polarization is invariant with respect to twinning. Another possibility is for P' to point towards 100 (red index) instead of $\bar{1}00$ (red index). Then, the out-of-plane polarization would be affected whereas the in-plane polarization would remain invariant. In conclusion: Twining affect the macroscopic net polarization of the film.

V. CONCLUSION

CSD was demonstrated to be a viable route to produce high-quality epitaxial BTO films on (100), (110), and (111) oriented STO substrates. The films were relaxed by edge dislocations, which are semi-periodically spaced across the substrate-film interface. The most frequently observed Burgers vectors were determined as $a\langle 010\rangle$, $a[1\bar{1}0]$ and $a[001]$, and $a\langle 110\rangle$, for the (100), (110), and (111) film, respectively. The films are under tensile strain due to the difference in thermal expansion between STO and BTO. Comparing the measured dislocation distances to the theoretical values calculated based on the Burgers vectors, it was demonstrated that the films are fully relaxed by the introduction of the dislocations. In the (100) and (110) films only pure edge dislocations were observed, whereas a Burgers vector with both an edge component and a screw component was observed in the (111) film. The Sr/Ba interdiffusion distance at the interface was measured by EELS to be 3.4, 5.3, and 5.3 nm for the (100), (110), and (111) oriented films, respectively. Based on Ba-cation diffusion in BTO and Sr-cation diffusion in STO, the interdiffusion width is of expected size. It was demonstrated that the boundary between each spin coated layer of BTO was Ba-deficient, meaning that BaO is volatile at 1000 °C during thermal processing of the BTO films. In case of the (111) film, an APB and a thin twin crystal was observed at the boundary between each spin coated layer, as well as a grain with a twin crystal structure growing all the way to the surface. The APB is suggested to accommodate charge imbalance at the highly defective surface, and twins can minimize the macroscopic polarization of the film.

SUPPLEMENTARY MATERIAL

See supplementary material for SEM images of the film surfaces (Fig. S1), BF-STEM images of dislocation densities in the (110) and (111) film (Fig. S2) , EELS scans across Ba-deficient boundaries (Fig. S3), and SADPs from multiple sites within the films (Fig. S4, S5, and S6).

AUTHOR'S CONTRIBUTIONS

IEN performed all the TEM work with supervision from PEV and TG. TR synthesized the films. IEN wrote the manuscript under supervision of TG and with contributions from all the authors.

ACKNOWLEDGEMENTS

The Research Council of Norway is acknowledged for financial support through the projects FASTS (250403/F20) and BORNIT (275139/F20), and for support to the Norwegian Micro- and Nano-Fabrication Facility, NorFab (295864) and to the Norwegian Center for Transmission Electron Microscopy, NORTEM (197405/F50). The authors would also like to acknowledge professor Mari-Ann Einarsrud for proof reading the manuscript.

AVAILABILITY OF DATA

The data that support the findings of this study are available from the corresponding author upon reasonable request.

REFERENCES

[1] J. F. Scott, "Applications of modern ferroelectrics," Science **315**, 954–959 (2007).
[2] D. Taylor, "Thermal expansion data. VIII: Complex oxides, ABO_3, the perovskites," Transactions and Journal of the British Ceramic Society (1985).
[3] Z. X. W. Yung H. Hu, Helen M. Chan and M. P. Harmer, "Scanning electron microscopy and transmission electron microscopy study of ferroelectric domains in doped $BaTiO_3$," Journal of the American Ceramic Society **69**, 594–602 (1986).
[4] A. S. Everhardt, T. Denneulin, A. Grünebohm, Y.-T. Shao, P. Ondrejkovic, S. Zhou, N. Domingo, G. Catalan, J. Hlinka, J.-M. Zuo, S. Matzen, and B. Noheda, "Temperature-independent giant dielectric response in transitional $BaTiO_3$ thin films," Applied Physics Reviews **7**, 011402 (2020).
[5] T. Suzuki, Y. Nishi, and M. Fujimoto, "Analysis of misfit relaxation in heteroepitaxial $BaTiO_3$ thin films," Philosophical Magazine A **79**, 2461–2483 (1999).
[6] T. M. Raeder, K. Bakken, J. Glaum, M. A. Einarsrud, and T. Grande, "Enhanced in-plane ferroelectricity in $BaTiO_3$ thin films fabricated by aqueous chemical solution deposition," AIP Advances **8**, 105228 (2018).
[7] B. I. Edmondson, S. Kwon, C. H. Lam, J. E. Ortmann, A. A. Demkov, M. J. Kim, and J. G. Ekerdt, "Epitaxial, electro-optically active barium titanate thin films on silicon by chemical solution deposition," Journal of the American Ceramic Society **103**, 1209–1218 (2019).
[8] D. G. Schlom, L.-Q. Chen, C.-B. Eom, K. M. Rabe, S. K. Streiffer, and J.-M. Triscone, "Strain tuning of ferroelectric thin films," Annual Review of Materials Research **37**, 589–626 (2007).
[9] A. R. Damodaran, J. C. Agar, S. Pandya, Z. Chen, L. Dedon, R. Xu, B. Apgar, S. Saremi, and L. W. Martin, "New modalities of strain-control of ferroelectric thin films," Journal of Physics: Condensed Matter **28**, 263001 (2016).
[10] K. J. Choi, M. Biegalski, Y. L. Li, A. Sharan, J. Schubert, R. Uecker, P. Reiche, Y. B. Chen, X. Q. Pan, V. Gopalan, L.-Q. Chen, D. G. Schlom, and C. B. Eom, "Enhancement of ferroelectricity in strained $BaTiO_3$ thin films," Science **306**, 1005–1009 (2004).
[11] T. M. Raeder, T. S. Holstad, I.-E. Nylund, M.-A. Einarsrud, J. Glaum, D. Meier, and T. Grande, "Anisotropic in-plane dielectric and ferroelectric properties of tensile-strained $BaTiO_3$ films with three different crystallographic orientations," AIP Advances **11**, 025016 (2021).
[12] F. D. L. Peña, E. Prestat, V. T. Fauske, P. Burdet, P. Jokubauskas, M. Nord, T. Ostasevicius, K. E. MacArthur, M. Sarahan, D. N. Johnstone, J. Taillon, J. Lähnemann, V. Migunov, A. Eljarrat, J. Caron, T. Aarholt, S. Mazzucco, M. Walls, T. Slater, F. Winkler, Pquinn-Dls, B. Martineau, G. Donval, R. McLeod, E. R. Hoglund, I. Alxneit, D. Lundeby, T. Henninen, Luiz Fernando Zagonel, and A. Garmannslund, "hyperspy/hyperspy: Hyperspy v1.5.2," (2019).
[13] P. Virtanen, R. Gommers, T. E. Oliphant, M. Haberland, T. Reddy, D. Cournapeau, E. Burovski, P. Peterson, W. Weckesser, J. Bright, S. J. van der Walt, M. Brett, J. Wilson, K. J. Millman, N. Mayorov, A. R. J. Nelson, E. Jones, R. Kern, E. Larson, C. J. Carey, İ. Polat, Y. Feng, E. W. Moore, J. VanderPlas, D. Laxalde, J. Perktold, R. Cimrman, I. Henriksen, E. A. Quintero, C. R. Harris, A. M. Archibald, A. H. Ribeiro, F. Pedregosa, and P. van Mulbregt, "SciPy 1.0: fundamental algorithms for scientific computing in python," Nature Methods **17**, 261–272 (2020).
[14] J. D. Hunter, "Matplotlib: A 2d graphics environment," Computing in Science & Engineering **9**, 90–95 (2007).

[15] Y. B. Xu, Y. L. Tang, Y. L. Zhu, Y. Liu, S. Li, S. R. Zhang, and X. L. Ma, "Misfit strain relaxation of ferroelectric $PbTiO_3$/$LaAlO_3$ (111) thin film system," Scientific Reports **6** (2016), 10.1038/srep35172.

[16] R. Sažinas, I. Sakaguchi, M.-A. Einarsrud, and T. Grande, "^{134}Ba diffusion in polycrystalline $BaMO_3$ (M = Ti, Zr, Ce)," AIP Advances **7**, 115024 (2017).

[17] K. Gömann, G. Borchardt, M. Schulz, A. Gömann, W. Maus-Friedrichs, B. Lesage, O. Kaïtasov, S. Hoffmann-Eifert, and T. Schneller, "Sr diffusion in undoped and la-doped SrTiO3single crystals under oxidizing conditions," Phys. Chem. Chem. Phys. **7**, 2053–2060 (2005).

[18] K. Bakken, A. B. Blichfeld, D. Chernyshov, T. Grande, J. Glaum, and M.-A. Einarsrud, "Mechanisms for texture in $BaTiO_3$ thin films from aqueous chemical solution deposition," Journal of Sol-Gel Science and Technology **95**, 562–572 (2020).

[19] Y. Ikuhara and P. Pirouz, "High resolution transmission electron microscopy studies of metal/ceramics interfaces," Microscopy Research and Technique **40**, 206–241 (1998).

[20] Y. Tang, Y. Zhu, H. Meng, Y. Zhang, and X. Ma, "Misfit dislocations of anisotropic magnetoresistant $Nd_{0.45}Sr_{0.55}MnO_3$ thin films grown on $SrTiO_3$ (110) substrates," Acta Materialia **60**, 5975–5983 (2012).

[21] P. Langjahr, F. Lange, T. Wagner, and M. Rühle, "Lattice mismatch accommodation in perovskite films on perovskite substrates," Acta Materialia **46**, 773–785 (1998).

[22] C. L. Jia, S. B. Mi, K. Urban, I. Vrejoiu, M. Alexe, and D. Hesse, "Effect of a single dislocation in a heterostructure layer on the local polarization of a ferroelectric layer," Physical Review Letters **102** (2009), 10.1103/physrevlett.102.117601.

[23] R. Sažinas, I. Sakaguchi, I. Hasle, J. M. Polfus, R. Haugsrud, M.-A. Einarsrud, and T. Grande, "Tracer diffusion of ^{96}Zr and ^{134}Ba in polycrystalline $BaZrO_3$," Physical Chemistry Chemical Physics **19**, 21878–21886 (2017).

[24] R. Sažinas, C. Bernuy-López, M.-A. Einarsrud, and T. Grande, "Effect of CO_2 exposure on the chemical stability and mechanical properties of $BaZrO_3$-ceramics," Journal of the American Ceramic Society **99**, 3685–3695 (2016).

[25] R. Sažinas, M.-A. Einarsrud, and T. Grande, "Toughening of y-doped $BaZrO_3$ proton conducting electrolytes by hydration," Journal of Materials Chemistry A **5**, 5846–5857 (2017).

[26] S. M. Selbach, M.-A. Einarsrud, T. Tybell, and T. Grande, "Synthesis of $BiFeO_3$ by wet chemical methods," Journal of the American Ceramic Society **90**, 3430–3434 (2007).

[27] M. Kosec, B. Malic, and M. Mandeljc, "Chemical solution deposition of PZT thin films for microelectronics," Materials Science in Semiconductor Processing **5**, 97–103 (2002).

[28] N. H. Gaukås, S. M. Dale, T. M. Ræder, A. Toresen, R. Holmestad, J. Glaum, M.-A. Einarsrud, and T. Grande, "Controlling phase purity and texture of $K_{0.5}Na_{0.5}NbO_3$ thin films by aqueous chemical solution deposition," Materials **12**, 2042 (2019).

[29] K. P. Fahey, B. M. Clemens, and L. A. Wills, "Nonorthogonal twinning in thin film oxide perovskites," Applied Physics Letters **67**, 2480–2482 (1995).